electronics

MDPI

Article

Fuzzy Logic-Based Direct Power Control Method for PV Inverter of Grid-Tied AC Microgrid without Phase-Locked Loop

Shameem Ahmad [1], Saad Mekhilef [1,2,*], Hazlie Mokhlis [1,*], Mazaher Karimi [3,*], Alireza Pourdaryaei [4,5], Tofael Ahmed [6], Umme Kulsum Jhuma [1] and Suhail Afzal [1,7]

1 Power Electronics and Renewable Energy Research Laboratory (PEARL), Department of Electrical Engineering, Universiti Malaya, Kuala Lumpur 50603, Malaysia; ahmad05shameem@gmail.com (S.A.); umme.jr@gmail.com (U.K.J.); suhailafzal@bzu.edu.pk (S.A.)
2 School of Science, Computing and Engineering Technologies, Swinburne University of Technology, Hawthorn, VIC 3122, Australia
3 School of Technology and Innovations, University of Vaasa, Wolffintie 34, FI-65200 Vaasa, Finland
4 Department of Power and Control, School of Electrical and Computer Engineering, Shiraz University, Shiraz 7194684334, Iran; a.pourdaryaei@gmail.com
5 Department of Electrical and Computer Engineering, University of Hormozgan, Bandar Abbas 7916193145, Iran
6 Department of Electrical and Electronic Engineering, Chittagong University of Engineering and Technology, Chittagong 4349, Bangladesh; tofael@cuet.ac.bd
7 Department of Electrical Engineering, Faculty of Engineering and Technology, Bahauddin Zakariya University, Multan 60800, Pakistan
* Correspondence: saad@um.edu.my or smekhilef@swin.edu.au (S.M.); hazli@um.edu.my (H.M.); mazaher.karimi@uwasa.fi (M.K.)

check for updates

Citation: Ahmad, S.; Mekhilef, S.; Mokhlis, H.; Karimi, M.; Pourdaryaei, A.; Ahmed, T.; Jhuma, U.K.; Afzal, S. Fuzzy Logic-Based Direct Power Control Method for PV Inverter of Grid-Tied AC Microgrid without Phase-Locked Loop. *Electronics* **2021**, *10*, 3095. https://doi.org/10.3390/electronics10243095

Academic Editors: Shailendra Rajput, Moshe Averbukh and Noel Rodriguez

Received: 14 November 2021
Accepted: 10 December 2021
Published: 13 December 2021

Abstract: A voltage source inverter (VSI) is the key component of grid-tied AC Microgrid (MG) which requires a fast response, and stable, robust controllers to ensure efficient operation. In this paper, a fuzzy logic controller (FLC)-based direct power control (DPC) method for photovoltaic (PV) VSI was proposed, which was modelled by modulating MG's point of common coupling (PCC) voltage. This paper also introduces a modified grid synchronization method through the direct power calculation of PCC voltage and current, instead of using a conventional phase-locked loop (PLL) system. FLC is used to minimize the errors between the calculated and reference powers to generate the required control signals for the VSI through sinusoidal pulse width modulation (SPWM). The proposed FLC-based DPC (FLDPC) method has shown better tracking performance with less computational time, compared with the conventional MG power control methods, due to the elimination of PLL and the use of a single power control loop. In addition, due to the use of FLC, the proposed FLDPC exhibited negligible steady-state oscillations in the output power of MG's PV-VSI. The proposed FLDPC method performance was validated by conducting real-time simulations through real time digital simulator (RTDS). The results have demonstrated that the proposed FLDPC method has a better reference power tracking time of 0.03 s along with reduction in power ripples and less current total harmonic distortion (THD) of 1.59%.

Keywords: microgrid; PLL; RTDS; direct power control; fuzzy logic; voltage source inverter

1. Introduction

Fossil fuel resources are frequently used to generate power in conventional power systems, which outcomes in the hasty diminution of fossil fuel, as well as augmented environmental pollution. Renewable energy has arisen as an alternate solution to overcome the environmental and fossil fuel scarcity issues around the world. As a result, modern power systems have undergone vast changes and up-gradation to accommodate renewable energy sources in the power system network. The microgrid (MG) is one of such revolutions, integrating dispatchable and non-dispatchable distributed generation (DG) units through

power electronics devices to power system networks, and providing uninterruptible power to communities [1,2]. MG possesses benefits like low capital cost, a low payback period, and high reliability; however, regarding their operation, there are still numerous technical challenges, including the flexible control of power flow between the utility grid and MG during grid-tied mode, and voltage magnitude and frequency control during islanding operation [3]. In this study, the control strategy that governs the smooth flow of real and reactive power between the MG and the utility grid for efficient operation of grid-tied AC-MG, with multiple DGs, is considered.

Grid-tied voltage source inverters (VSI) are one of the key devices of a MG, which interconnect the DG units of the MG with the main grid, and regulate power flow between them by adopting appropriate power control methods. It has become very important for grid-tied VSI to ensure high power quality and stability, as the penetration level of MG renewable energy resources in modern power grids is increased. The power controllers allow the MG system to attain a fast response and a small steady state rate of error, and to maintain stability during drastic changes [4]. A rotating synchronous reference frame-based trajectory current control scheme is the commonly used strategy to control the output power of a grid-tied VSI. In this scheme, by regulating dq axes currents separately, real and reactive powers are controlled where the decoupling-term-based linear proportional integral (PI) controller can be applied indirectly [4].

To ensure better efficiency, reliability and safety of VSIs used in grid-tied MGs, in the literature based on dq current control schemes (CCSs), various real and reactive power control methods have been proposed. Worku et al. proposed a power control strategy for photovoltaic (PV) and battery storage-based AC-MGs, based on decoupled dq CCS [5]. A rigid power controller was proposed by Safa et al. for a grid-connected VSI, to improve AC-MG power quality [6]. A new power control method, based on the artificial neural network (ANN) to control the power quality of PV-incorporated AC-MGs, was presented by Kaushal et al. [7]. For controlling the VSI of a grid-tied AC-MG, Smadi et al. proposed a compact control strategy based on dq CCS [8]. By cascading the voltage and current controller, a new power control scheme was proposed by Lou et al. for an AC-MG VSI [9]. A power control strategy, based on a sliding mode-integrated dq CCS, was proposed by Abadlia et al. for a hybrid grid-tied PV/hydrogen system [10]. Based on an instantaneous self-tuning technique, another power control scheme was designed by Feng et al. for a grid-tied MG [11]. Adhikari et al., for a maximum power point tracking (MPPT) system-integrated hybrid PV/battery system, proposed a coordinated power control strategy [12]. A coupled harmonic compensation and voltage support method was developed by Mousavi et al., for DG-interfaced VSIs in grid-tied AC-MGs [13]. To regulate the power flow between grid and PV/battery hybrid systems, Go et al. proposed a power control strategy for VSI [14]. A power control and management system for a grid-tied MG was developed by Sedaghati to ensure the optimum operation of MG [15]. For controlling the output power of grid-tied PV-VSI in AC-MGs, a voltage-oriented power coordination strategy was proposed by Tang et al. [16]. A dq axes CCS synchronous reference frame-based power control method was proposed by Ahmad et al. for grid-connected AC-MG's VSIs [17].

Since in the aforementioned methods, Park's transformation has been used during abc to dq transformation, there is a need for phase angle extraction from grid voltages to ensure dq axes currents and grid voltages are in phase with each other [18]. Phase-locked loop (PLL) systems are commonly used for the extraction of grid voltage phase angles, based on arctangent functions [19]. However, the problems with the use of PLL systems are their adverse impact on VSIs' small-signal stability, along with the slowdown of the transient response of the power system parameters, causing high ripples in real and reactive power [20]. Moreover, at low frequencies PLL initiates negative resistance, which deteriorates VSIs stability [21]. PLL also introduces dynamic coupling in VSIs [22]. Furthermore, the power system's dynamic performance is also jeopardized, due to the adoption of low-bandwidth PLLs for improving VSIs' stability and robustness. Another

issue associated with all these controllers is the consideration of two control loops, namely the outer power and inner current control loops, when designing the power control scheme. Due to the presence of two control loops, the computation burden increases. Furthermore, the performances of the above-mentioned control methods are greatly influenced by the accurate tuning of PI controller gains, the conditions of grid voltage, and the comprehensiveness of the current decoupling [23]. In addition, PI controllers cannot eliminate steady state error for sinusoidal signals, and they cannot handle power system non-linearity efficiently. Moreover, due to the existence of multivariable parameters, during dynamic-load variations PI controllers have a poorer performance [24].

In some studies, fuzzy logic controller (FLC)-based control methods have been proposed for VSIs operating in grid-tied or autonomous modes for DG applications. Hasanien et al. proposed an FLC-based control method to maintain the output voltage of VSI for the islanded DG system during load variability and weather uncertainties [24]. A type-2 FLC-based control method was developed by Heydari et al. for VSIs of autonomous naval shipboard microgrids, to damp the steady-state deviations of voltage and frequency [25]. However, in [24,25], FLC controllers were used to control the output voltage and frequency of VSIs during an islanded operation. Thao et al. developed a power control method by combining feedback linearization and FLC, to reduce the fluctuations in the VSI's output active and reactive powers at the steady state, for a grid-tied PV system [26]. Another FLC-based power control method was proposed by Omar et al. to control the output power of grid-connected PV-VSI [27]. Jamma et al. proposed an FLC and ANN combined DPC for controlling the VSI output power of a grid-tied PV system [28]. For a grid-tied PV system VSI, a control method based on FLC and the Levenberg–Marquardt optimization method was proposed by Islam et.al. [29]. Shadoul et.al. proposed an adaptive FLC-based control method for grid-tied PV-VSIs [30]. FLC-based active and reactive power control was proposed by Tahri et al. for a grid-tied PV system's neutral-point-clamped VSI [31]. Teekaraman et al. developed an FLC-based current control method for a grid-tied Z-source VSI [32]. In all these studies [26–32], even though FLC was considered when designing the feedback controller, all the control methods were based on dq CCS where Park Transformation was used for abc to dq transformation, and PLL was implemented to extract the voltage angle. As mentioned earlier, due to the use of the PLL system, the control methods performance deteriorated, and most of the control methods consisted of two control loops. As a result, undesirable ripples were observed in the VSI output powers, and controllers took a longer time to track the reference powers. Furthermore, the performance of all these controllers were validated only for grid-tied PV systems, which are not connected to MGs.

To overcome the issue of double control loops, direct power control (DPC) method was introduced for VSI, where the inner current control loop was omitted. A control method for VSI based on a DPC, to control the output power, was introduced by Gui et al. [33,34]. However, due to the use of the variable switch frequency in this method, undesirable harmonics occurred, which hampered the suitable design of the line filter. The DPC method based on the sliding mode and model predictive controllers were introduced by Gui et al. [35] and Choi et al. [36], respectively, to improve the fast tracking of power references and DPC method robustness. Though power tracking performance was improved, undesirable ripples still existed in real and reactive power, and their performances were not validated for MG applications.

In this paper, to address the problems associated with the previous power controllers of PV-VSI, an FLC-based DPC (FLDPC) method is proposed for AC-MG's photovoltaic (PV) VSI, through modulating MG's point of common coupling (PCC) voltage. The advantages of FLC over conventional PI controllers, is that their design is independent of power system mathematical modelling, and can therefore deal with power system non-linearities effectively, and can easily adopt the dynamic load variation of a power system [24]. For grid-synchronization, instead of using a PLL system, in this study, the direct power calculation of PCC voltage and current grid-synchronization takes place. The proposed FL-DPC method also consists of a feedforward decoupled control, and a feedback FLC method

including the non-linear voltage modulated control. Since the proposed controller excludes Park transformation and PLL, it exhibits a faster and more transient dynamic performance, compared with conventional PLL-PI-integrated CCS-based power control methods. In addition, due to the use of FLC and the elimination of PLL, the steady state oscillation in VSI output power reduced substantially, and the reference power tracking speed became faster. Furthermore, the computational burden was also reduced, since the proposed FLDPC had only a single power control loop, which regulated the instantaneous real and reactive power flow, directly. Moreover, the presence of the feedforward decoupled control eliminated the coupling terms presented in the new control inputs from the nonlinear PCC voltage modulation (PVM), and finally, two individual dynamics of the second order error signals of the real and reactive were obtained, using a feedback FLC strategy. For controlling the bus voltage and frequency of the MG during islanded mode of operation, a V-f control strategy was adopted [37].

The main contribution of this paper is unlike conventional CCS-based VSI; the PV-VSI is modelled based on DPC and PVM theory (PVMT) to control the real and reactive power flow between the AC-MG and the utility grid. The detailed mathematical modelling of the grid synchronization technique, based on the direct power calculation of PCC voltage and current was conducted. The modelling of the FLDPC strategy for PV-VSI, along with feedforward decoupled control is also depicted extensively. Real-time simulations were carried out using a real-time digital simulator (RTDS) for different references of real and reactive power, to test the proposed FLDPC method's performance. Considering real-world scenarios, the performance of the proposed controller was verified by changing the PV generation and load demand simultaneously, during both MG's grid-tied and islanded modes of operation. Finally, to demonstrate the pre-eminence of the proposed FLDPC controller, real-time simulations of different conventional grid-tied MG power control methods were conducted, and their performances were compared with the proposed controller for various parameters of steady-state power oscillations, refence power tracking time and total harmonic distortions (THD) of VSI's output current and voltage.

The organization of the rest of the paper is as follows: in Section 2, the modelling of AC-MG's different components are presented. In Section 3, the mathematical modelling of the DPC and PVMT-based VSI are presented. Section 4 presents the proposed FLDPC method's design strategy. Section 5 presents the results obtained through the real-time simulations, along with a detailed discussion and comparative study. Finally, a conclusion of this study is presented in Section 6.

2. Configuration of AC Microgrid Testbed

The grid-tied AC-MG testbed used in this study consisted of a PV system, a battery storage, a diesel generator and two types of load (critical and non-critical) which is represented in Figure 1. The modelling of the MG was conducted in an RSCAD platform, using modules of different components available in the RSCAD library. In Appendix A Table A1, the specifications of all the components used in the MG are depicted, which were obtained from [38]. As shown in Figure 1, two VSIs are used to connect the PV and battery storage systems with the AC bus, and the AC-MG was integrated with the grid through a 3-ph transformer.

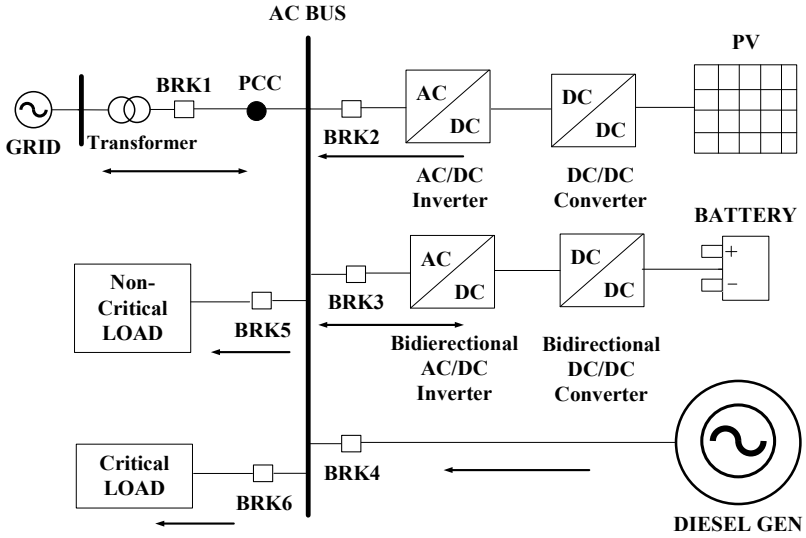

Figure 1. Schematic of Modelled Grid-tied AC Microgrid.

2.1. Photovoltaic (PV) System

The 0.1 MW-rated PV system used in this study, and the parameters of the system, are depicted in Table A1. To control the output of the PV-VSI, a PVMT-based FLDPC strategy was developed, which is described in Sections 3 and 4.

The relationship between the PV system's current and voltage can be represented as follows:

$$I_{PV} = I_{ph} - I_D - I_{sh} = I_{ph} - I_0[\exp \frac{q}{AKT(V_{PV} + I_{PV}R_s)} - 1] - \frac{V_{PV} + I_{PV}R_s}{R_{sh}} \quad (1)$$

where cell output voltage is V_{PV}, cell output current is I_{PV}, diode current is I_D, photocurrent is I_{ph}, reverse saturation current is I_0, electron charge is q, shunt resistance current is I_{sh}, temperature of cell is T, shunt resistance R_{sh}, series resistance R_s and quality factor is A.

A modified incremental conductance algorithm-based MPPT controller [39] is implemented to extract maximum power from the PV system. By using (2), the maximum power can be determined:

$$P_{pv}(t) = \eta_{pv} A_c I(t)(1 - 0.005(T_0(t) - 25)) \quad (2)$$

where cell array area is A_c, PV system efficiency is η_{pv}, solar irradiation is I and ambient temperature is T_0.

2.2. Battery Storage System (BSS)

In this study, the battery storage system (BSS) is comprised of strings of lithium-ion battery, a bidirectional DC-AC VSI, and a bidirectional DC-DC buck-boost converter. A control technique proposed in [5] was employed in this study to control the battery VSI. The size of the battery was chosen based on the critical load demand, so that in the case of any contingency the battery was able to provide back up. In charging mode, battery charged either by PV (power generation of PV is more than demand) or via the grid in grid-tied mode. In contrast, the battery operated in discharge mode when the MG was islanded, or the generation of PV was less than its capacity in grid-tied mode.

The crucial parameters of the battery are terminal voltage and SOC, which can be calculated based on (3) and (4) [40]:

$$V_{bat} = i_{bat}R_{bat} + V_{oc} + V_e e^{B\int i_{bat}dt} - k\frac{Ah}{Ah + \int i_{bat}dt} \quad (3)$$

$$SOC = \left(1 + \frac{\int i_{bat}dt}{Ah}\right) * 100 \quad (4)$$

where open circuit voltage is V_{oc}, terminal voltage of the battery is V_{bat}, battery internal resistance is R_{bat}, battery current is i_{bat}, exponential voltage is V_e, polarization voltage is k and B is the exponential capacity.

2.3. Diesel Generator

In this study, a diesel generator was used to provide backup supply to the MG when the grid fails. It comprised a diesel engine, a synchronous machine, and for regulating the machine's speed and frequency, an excitation system-driven speed governor. The modelling of the three different parts of the diesel generator was adopted from [41]. The dynamics of each diesel generator components can be given by (5) and (8).

The governor control system transfer function:

$$H_c = \frac{K_1(T_3 s + 1)}{(T_1 T_2 s^2 + T_1 s + 1)} \tag{5}$$

where, H_c is the transfer functions of governor control system, K_1 is the transfer function constants, and T_1 to T_3 are the time constants.

Actuator Transfer function:

$$H_a = \frac{(T_4 s + 1)}{s(T_5 s + 1)(T_6 s + 1)} \tag{6}$$

where H_a is the transfer functions actuator, and T_4 to T_6 are the time constants.

Diesel engine transfer function:

$$H_{eng} = e^{-T_D s} \tag{7}$$

where governor control system transfer functions is H_{eng} is and T_D is the time constant.

Excitation system transfer function:

$$H_e = \frac{1}{(T_e s + K_e)} \tag{8}$$

where transfer function constant is K_e, exciter transfer function is H_e and time constant is T_e.

2.4. Grid

By using (3), the power absorbed or supplied by the grid can be calculated [40]:

$$P_g(t) = P_l(t) + \sum(P_{pv}(t), P_b(t)) \tag{9}$$

where grid supplied/absorbed is P_g, load power is P_l, battery power is P_b, and PV power is P_{pv}.

2.5. Load

To verify the performance of the proposed PLL-less FLDPC method, two types of load were considered in this study, namely, critical and non-critical load. The load values were chosen based on the MG generation capacity, which changed with respect to time.

3. DPC and PVMT-Based PV-VSI Modelling

In this section, the mathematical modelling of PV-VSI based on DPC and PVMT is presented. L-filters were used at the output of PV-VSI to reduce the harmonics in current and voltage. In Figure 2a,b, the schematics of the dq CCS-based control method with PLL and the proposed PVMT-based FLDPC method without PLL are presented respectively.

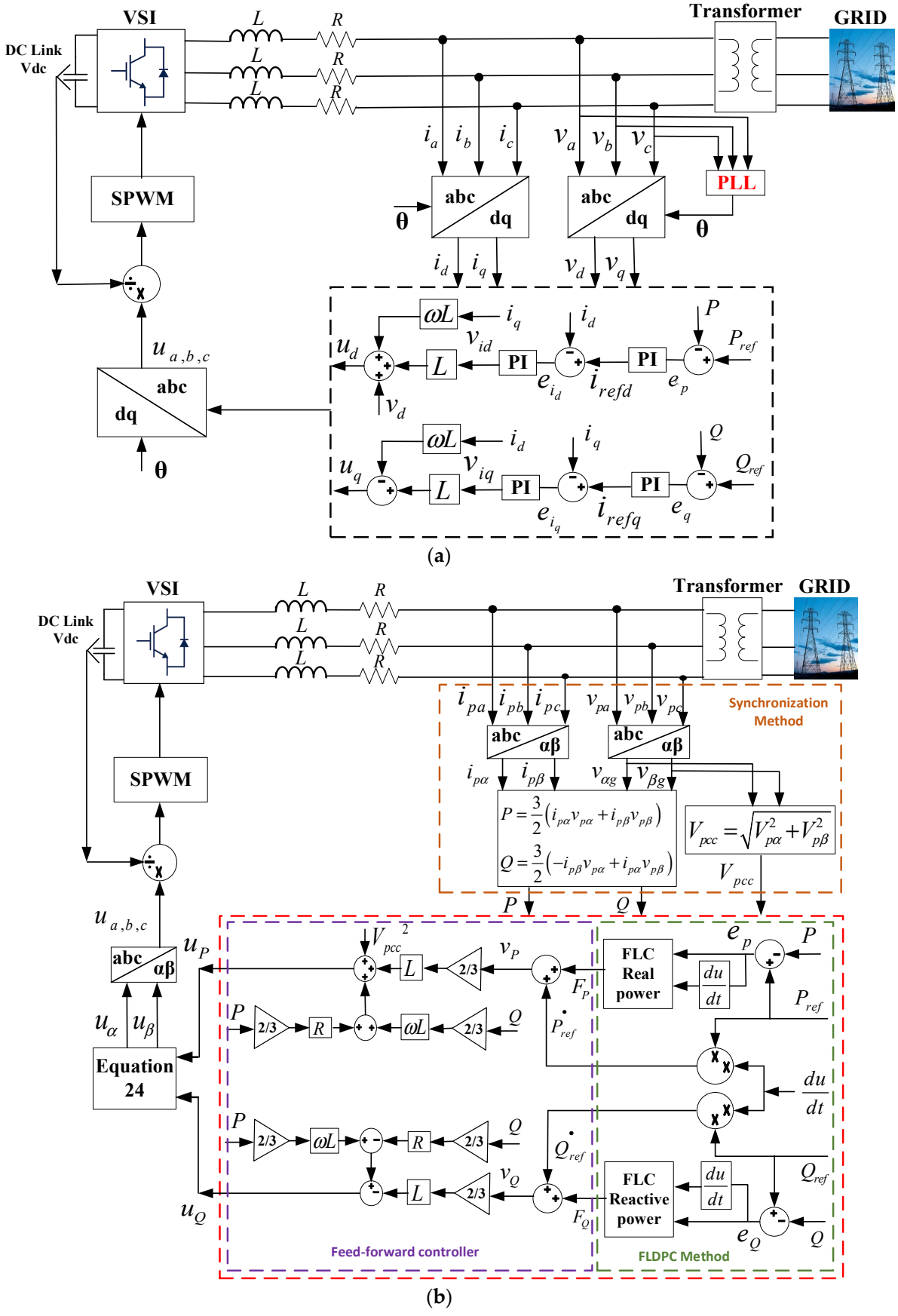

Figure 2. Power controllers for grid-tied AC-MG's PV-VSI, based on (**a**) PLL-PI-integrated dq CCS and (**b**) the proposed PVMT-based FLDPC.

The dynamic realtionships between VSI's output voltages, currents and PCC voltages can be represented using (10):

$$\begin{aligned} L\frac{di_{pa}}{dt} &= -v_{pa} + u_a - Ri_{pa} \\ L\frac{di_{pb}}{dt} &= -v_{bg} + u_b - Ri_{pb} \\ L\frac{di_{pc}}{dt} &= -v_{cg} + u_c - Ri_{pc} \end{aligned} \tag{10}$$

where, v_{pabc}, i_{pabc}, and u_{abc} are PCC voltages, VSI output currents and voltages, respectively. R and L are the resistance and inductance of filter, respectively.

The stationary reference frame of the equations presented in (10) can be transformed to (11) using Clarke's transformation:

$$\begin{aligned} L\frac{di_{p\alpha}}{dt} &= u_\alpha - v_{p\alpha} - Ri_{p\alpha} \\ L\frac{di_{p\beta}}{dt} &= u_\beta - v_{p\beta} - Ri_{p\beta} \end{aligned} \tag{11}$$

where PCC voltages are $u_{\alpha\beta}$, and VSI currents and voltages are $i_{p\alpha\beta}$ and $v_{p\alpha\beta}$, respectively, in α–β frame.

The stationary reference frame representation of instant reactive and real power flow between the utility grid and VSI can be presented as (12):

$$\begin{aligned} P &= \tfrac{3}{2}\left(i_{p\alpha}v_{p\alpha} + i_{p\beta}v_{p\beta}\right) \\ Q &= \tfrac{3}{2}\left(-i_{p\beta}v_{p\alpha} + i_{p\alpha}v_{p\beta}\right) \end{aligned} \tag{12}$$

where instant real and reactive powers supplied/injected by the grid are P and Q, respectively.

By differentiating (12), P and Q dynamic equations can be obtained as follows:

$$\begin{aligned} \frac{dP}{dt} &= \tfrac{3}{2}\left(v_{p\alpha}\frac{di_\alpha}{dt} + i_{p\alpha}\frac{dv_{p\alpha}}{dt} + v_{p\beta}\frac{di_{p\beta}}{dt} + i_{p\beta}\frac{dv_{p\beta}}{dt}\right) \\ \frac{dQ}{dt} &= \tfrac{3}{2}\left(-v_{p\alpha}\frac{di_{p\beta}}{dt} - i_{p\beta}\frac{dv_{p\alpha}}{dt} + v_{p\beta}\frac{di_{p\alpha}}{dt} + i_\alpha\frac{dv_{p\beta}}{dt}\right) \end{aligned} \tag{13}$$

For simplifying the dynamics of P and Q in the balanced grid condition, the relationship of the PCC α–β voltage can be obtained as given in (14):

$$\begin{aligned} v_{p\alpha} &= V_{pcc}\cos(\omega t) \\ v_{p\beta} &= V_{pcc}\sin(\omega t) \end{aligned} \tag{14}$$

where:

$$\begin{aligned} V_{pcc} &= \sqrt{{v_{p\alpha}}^2 + {v_{p\beta}}^2} \\ \omega &= 2\prod f \end{aligned} \tag{15}$$

where *PCC* voltage amplitude is V_{pcc}, angular frequency is ω and grid voltage frequency is f.

The dynamic equations of *PCC* voltages are obtained as (16) by differentiating (14).

$$\begin{aligned} \frac{dv_{p\alpha}}{dt} &= -\omega V_{pcc}\sin(\omega t) = -v_{p\beta}\omega \\ \frac{dv_{p\beta}}{dt} &= \omega V_{pcc}\cos(\omega t) = v_{p\alpha}\omega \end{aligned} \tag{16}$$

By substituting (10) and (16) in (13), the dynamic expression of real and reactive powers can be obtained as (17):

$$\begin{aligned} \frac{dp}{dt} &= \frac{3}{2L}\left(-{V_{pcc}}^2 + u_\alpha v_{p\alpha} + u_\beta v_{p\beta}\right) - \omega q - p\frac{R}{L} \\ \frac{dq}{dt} &= \frac{3}{2L}\left(-u_\beta v_{p\alpha} + u_\alpha v_{p\beta}\right) - \omega q - q\frac{R}{L} \end{aligned} \tag{17}$$

where, dynamic real and reactive power control inputs and outputs are (p and q) and (u_α and u_β), respectively.

Since both the control inputs in (17) are coupled in P and Q states, by using voltage modulation theory [34], the dynamics of (17) can be simplified as (18) to define new voltage modulated control inputs:

$$\begin{aligned} u_P &:= u_\alpha v_{p\alpha} + u_\beta v_{p\beta} \\ u_Q &:= u_\beta v_{p\alpha} - u_\alpha v_{p\beta} \end{aligned} \tag{18}$$

where the new control inputs are u_P and u_Q, and they are transformed into DC components as they satisfy (19):

$$\begin{bmatrix} u_P \\ u_Q \end{bmatrix} = V_{pcc}\begin{bmatrix} \cos(\omega t) & \sin(\omega t) \\ -\sin(\omega t) & \cos(\omega t) \end{bmatrix}\begin{bmatrix} u_\alpha \\ u_\beta \end{bmatrix} = V_{pcc}\begin{bmatrix} u_d \\ u_q \end{bmatrix} \tag{19}$$

where u_d and u_q are the *d-q* frame VSI voltages. Though the proposed method has no PLL system, the system is still presented in dq axis frame.

The dynamic expression of real and reactive powers presented in (17) can be expressed as (20), by substituting the control inputs of (17) with the new control inputs (u_P and u_Q).

$$\begin{aligned} \frac{dP}{dt} &= \frac{3}{2L}\left(-{V_{pcc}}^2 + u_P\right) - \omega Q - P\frac{R}{L} \\ \frac{dQ}{dt} &= \frac{3}{2L}u_Q - \omega Q - P\frac{R}{L} \end{aligned} \tag{20}$$

4. Controller Design

4.1. FLC-based Direct Power Control

In this section, for the new PVMT and DPC-based VSI model presented in (20), a robust and simple controller consisting of feedforward and feedback control structure is designed. In Figure 2, the FLDPC method's schematic for the PV-VSI is depicted. In this control, the power (real and reactive) references are tracked by controlling their actual value using FLC.

The real and reactive power errors can be obtained using (21):

$$\begin{aligned} e_P &:= P_{ref} - P \\ e_Q &:= Q_{ref} - Q \end{aligned} \tag{21}$$

where active and reactive power references are represented by P_{ref} and Q_{ref}, respectively, and real and reactive power errors are e_P and e_Q, respectively.

As shown in Figure 2, for obtaining zero steady state error, two error signals (e_P and e_Q) and their rate of change (*P-error_rate* and *Q-error_rate*) are given as inputs to two FLCs. The outputs of FLCs provided the control inputs F_P and F_Q for the feed-forward controllers. Due to non-availability of the FLC block in the RSCAD library, FLC is built in RSCAD software by writing codes using ANSI language in C-builder. Each FLC consisted of two inputs and one output, as depicted in Figure 2. The two inputs were the error and error-rates of power for each FLC. The membership functions of inputs and outputs were named identical for both real and reactive power. The variables representing error were NM (negative medium), ZV (zero value), and PM (positive medium). Similarly, error-rate variables were NM1 (negative medium 1), ZV1 (zero value 1), and PM1 (positive medium 1). The variables of output were BNE (big negative error), NME (negative medium error), ZE (zero error) and PME (positive medium error). In Figures 3 and 4, the real and reactive power FLCs' membership functions for error, error-rate and outputs are shown.

To ensure smooth control by FLC, triangular-based membership functions were considered in this study.

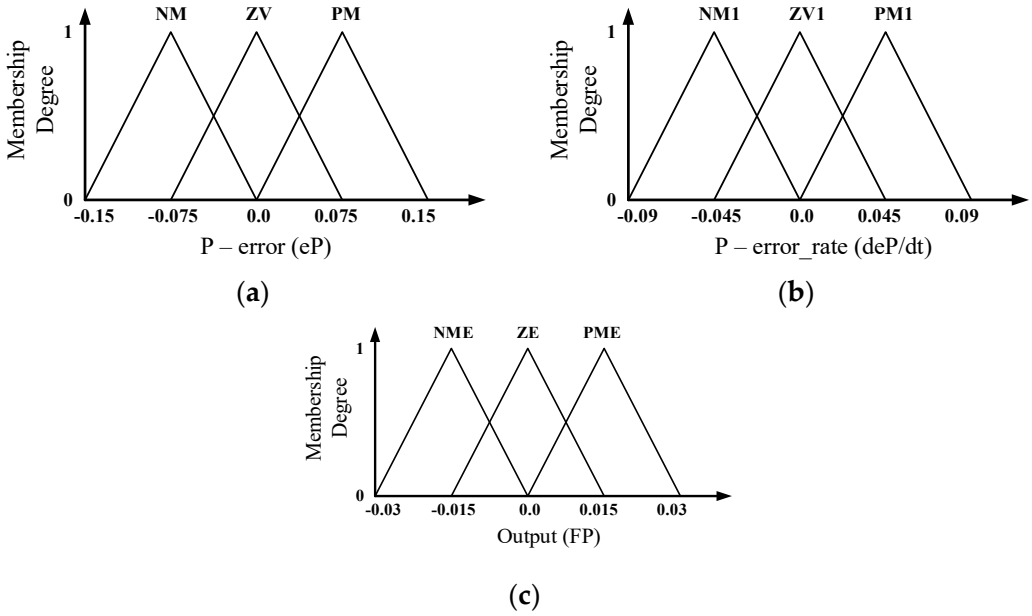

Figure 3. Membership functions of (**a**) P-error (e_P), (**b**) error_rate of P (de_P/dt) and (**c**) output of FLC (F_P).

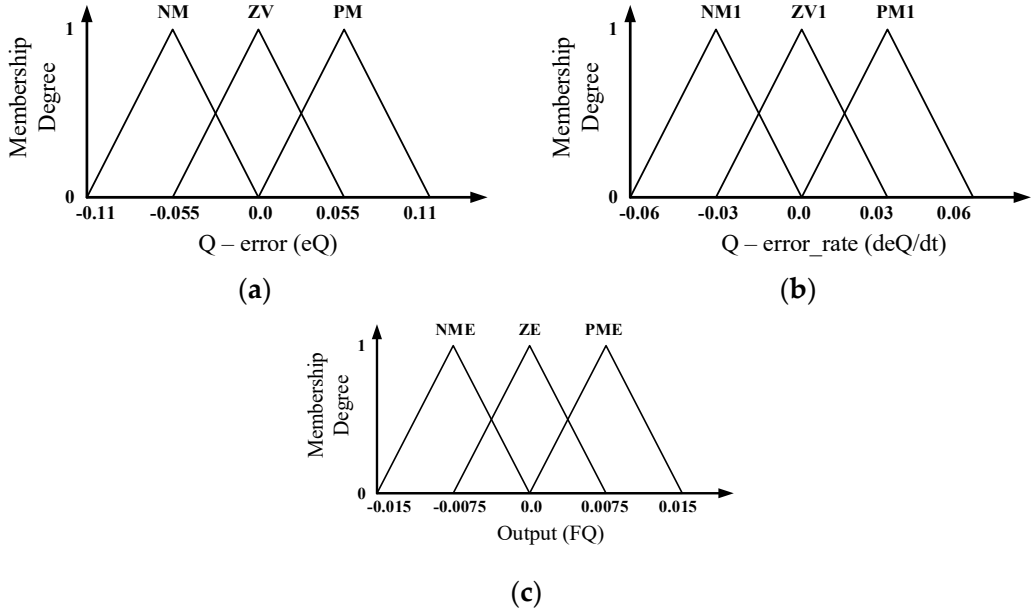

Figure 4. Membership functions of (**a**) Q-error (e_Q), (**b**) error_rate of Q (de_Q/dt) and (**c**) output of FLC (F_Q).

An important part in the design of FLC is choosing the scaling factors of input and output membership functions optimally. This can be obtained by implementing optimization techniques to minimize the deviation between inverter output powers and the reference powers. In this study, a black-box optimization technique known as the nonlinear Simplex method of Nelder and Mead is adopted for obtaining the optimal scaling factors of input and out membership functions [42]. The reason for choosing the black-box optimization technique is that it can be easily used in conjunction with time-domain or real-time simulation tools [24]. The process of black-box optimization entails the successive

evaluation of the objective function for the different sets of parameters for the membership functions. In this process, the real-time simulation program, i.e., RSCAD/RTDS, is used to evaluate the value of the objective function. First, an initial set of parameters was used to initialize the real-time simulation in RTDS, and the value of the objective function was numerically evaluated. Then, based on the optimization algorithm and the value of the objective function, a new set of parameters were obtained, and the process was repeated until an optimal set of parameters is determined.

To assign the input and output control, fuzzy rules were formed based on IF-THEN rules, which are summarized in Table 1. The rules were decided depending on the cooperation between the estimated error and complexity of FLC. In this paper, defuzzification was carried out by using the Sugeno-type weighted average method [43] to produce the real crisp output of F_P and F_Q.

Table 1. Rule table for FLCs of real and reactive power.

Membership Functions		ERROR RATE		
		NM1	**ZV1**	**PM1**
ERROR	**NM**	NME	NME	ZE
	ZV	NME	ZE	PME
	PM	ZE	PME	PME

4.2. Feed-Forward Controller

Due to the presence of coupling terms in the new MIMO system (20), and in this study, to eliminate the coupling terms, a feed-forward controller was designed, as expressed in (22):

$$\begin{aligned} u_P &= \tfrac{2}{3}Lv_P + \tfrac{2}{3}L\omega Q + \tfrac{2}{3}RP + {V_{pcc}}^2 \\ u_Q &= -\tfrac{2}{3}Lv_Q - \tfrac{2}{3}RQ + \tfrac{2}{3}L\omega P \end{aligned} \tag{22}$$

where feedback controller inputs are v_P and v_Q and can be calculated using (23):

$$\begin{aligned} v_P &= F_P + \dot{P}_{ref} \\ v_Q &= F_Q + \dot{Q}_{ref} \end{aligned} \tag{23}$$

where F_p and F_Q are the de-fuzzified output of the real and reactive power FLCs.

Finally, the genuine control inputs u_α and u_β were obtained using (24).

$$\begin{aligned} u_\alpha &= \tfrac{-u_Q v_{p\beta} + u_P v_{p\alpha}}{{V_{pcc}}^2} \\ u_\beta &= \tfrac{u_P v_{p\beta} + u_Q v_{p\alpha}}{{V_{pcc}}^2} \end{aligned} \tag{24}$$

These two control inputs using αβ-abc transformation were converted to 3-ph control signals, which were used to generate the control signals for the VSI switches using sinusoidal pulse width modulation (SPWM). SPWM was chosen in this study because the harmonics of lower and higher order can be reduced or eliminated easily using this technique.

4.3. Control of DC-Link Voltage

In Figure 5, the DC-link voltage controller is depicted, which aims to maintain a constant DC-link voltage during any disturbances or instabilities.

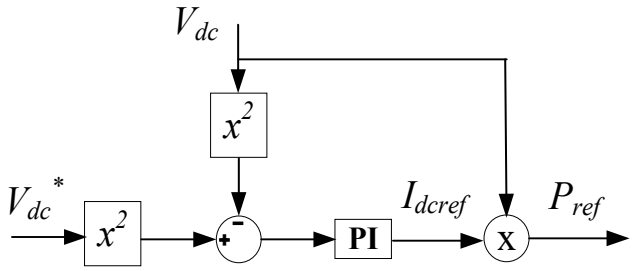

Figure 5. Schematic of controller of DC-link voltage.

The DC-link voltage error can be given by:

$$V_{dc\_error} = (V_{dc}{}^*)^2 - (V_{dc})^2 \tag{25}$$

where, $V_{dc}{}^*$ is the reference of V_{dc}.

To generate the DC current reference I_{dcref}, this error signal was sent to the PI controller to the ensure DC bus voltage constant value. The DC current reference I_{dcref} is given by:

$$I_{dcref} = K_{p,dc}\left((V_{dc}{}^*)^2 - (V_{dc})^2\right) + K_{i,dc}\int_0^t \left((V_{dc}{}^*)^2 - (V_{dc})^2\right)dt \tag{26}$$

where, $K_{p,dc}$ and $K_{i,dc}$ are the PI controller gains. In Appendix A Table A2, the PI controller gain values for DC-link voltage controller are presented.

5. Results

The real-time simulation results obtained through the implementation of the proposed PLL-less PVMT-based FLDPC method for PV-VSI of grid-tied MG are presented in this section. The real-time simulations were carried out on RTDS, and the laboratory setup to validate the performance of the proposed power controller is shown in Figure 6.

Figure 6. Laboratory setup of the proposed controller in AC MG with RTDS.

Two case studies were conducted in this study to validate the performance of the proposed power controller. For the first case study, the steady-state and transient response of the proposed controller for PV-VSI was validated by changing both real and reactive power references, and by changing only real power references. The results were compared with those of the conventional PLL-PI-integrated dq CCS-based control method, proposed in [6]. For the second case study, load demand and solar irradiation were varied to test the proposed controller performance during MG's different operating modes. Finally, a comparative study was conducted to prove the preeminence of the proposed FLDPC method.

5.1. Case 1: Change of Both Real and Reactive Power References

This section presents the results related to the power tracking performance of the proposed FLDPC method, and subsequently compares its performance with the PLL-PI-integrated dq CCS-based control method for both real and reactive power reference change.

5.1.1. Tracking Performance Analysis of the Proposed Controller

The results obtained for both the controllers tracking performance analysis are depicted in Figures 7 and 8. To test the tracking performance of the controller's real power, references were varied between 0 MW and 0.1 MW (PV output is non-linear), whereas reactive power references were changed between 0 MVar and 0.02 MVar, respectively.

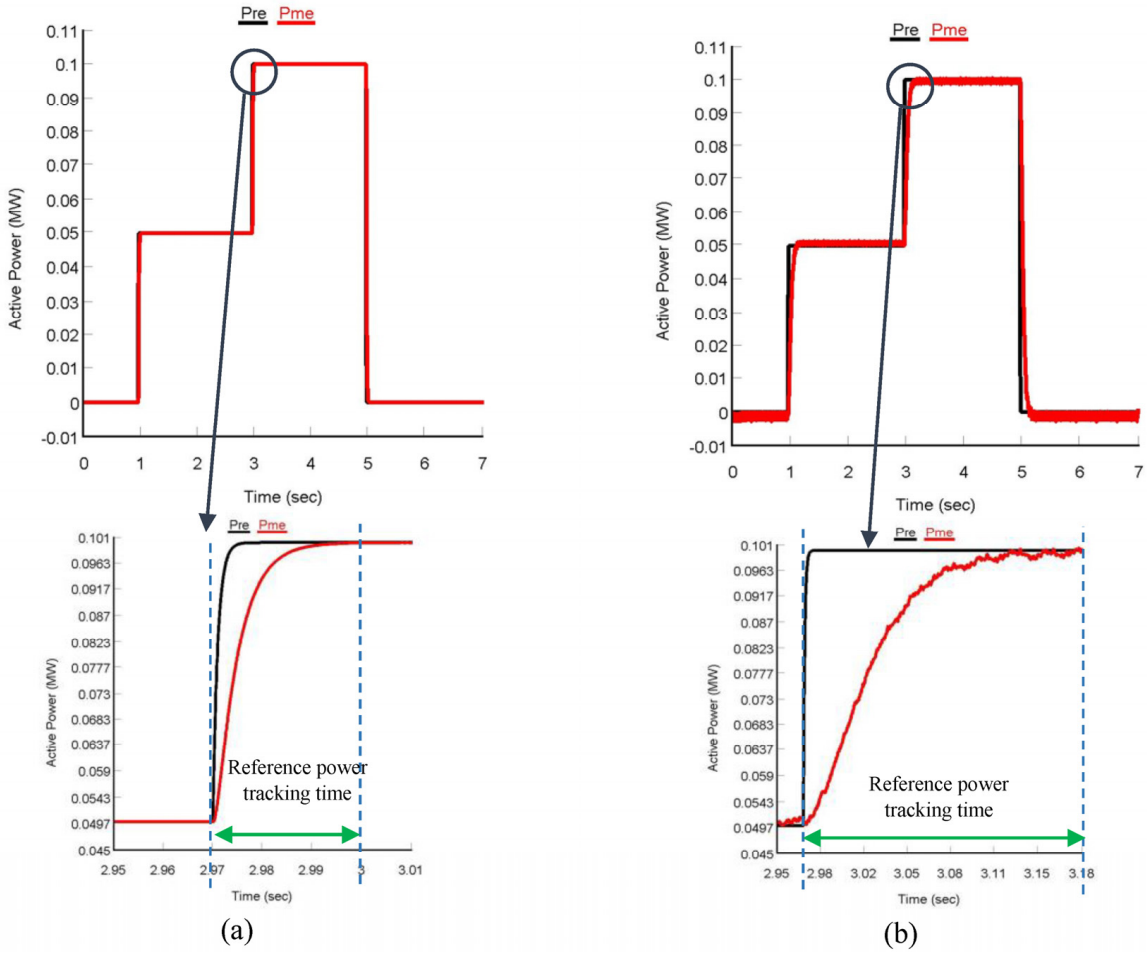

Figure 7. Real power tracking performance of (**a**) FLDPC method and (**b**) dq CCS-based power controller with PLL.

From Figure 7a, it is seen that, initially, real power reference was set to 0 MW, which was increased from 0 MW to 0.05 MW after 1 s. Then, it was set to 0.1 MW between 2.97 and 4.969 s, and the final reference was set to 0 MW again, between 4.97 and 7 s. For all the real power references, it was observed that the PV-VSI output real power, controlled by the proposed PVMT-based FLDPC, was tracking the real power references accurately. On the other hand, though from Figure 7b it seems that the conventional dq CCS-based power controller also tracked the reference powers, from the zoomed portion it is clear to see that the tracking speed of the proposed PLL-less PVMT-based FLDPC method is 0.03 s. This was 0.19 s faster than that of the conventional dq CCS-based power control method, whose real power reference tracking speed was 0.22 s. For reactive power, the reference power was kept to 0 MVar, initially, which increased to 0.01 MVar and 0.02 MVar at 1 s and 3 s, respectively. Finally, at 1 s reference reactive power decreased to 0 MVar. It can

be observed from Figure 8a that the VSI output reactive power controlled by the PVMT-based FLDPC method was following the reference reactive power accurately at different time intervals. In addition, the proposed PVMT-based FLDPC showed better tracking performance than that of CCS-based power controller, though the conventional CCS-based controller was able to track the reference reactive power, as shown in Figure 8b. According to the zoomed portion of Figure 8a,b, the time taken to reach a steady-state of reactive power by the proposed PVMT-based FLDPC was 0.03 s, where the conventional CCS-based power controller tracked it at 0.23 s. This was 0.20 s slower than the proposed controller.

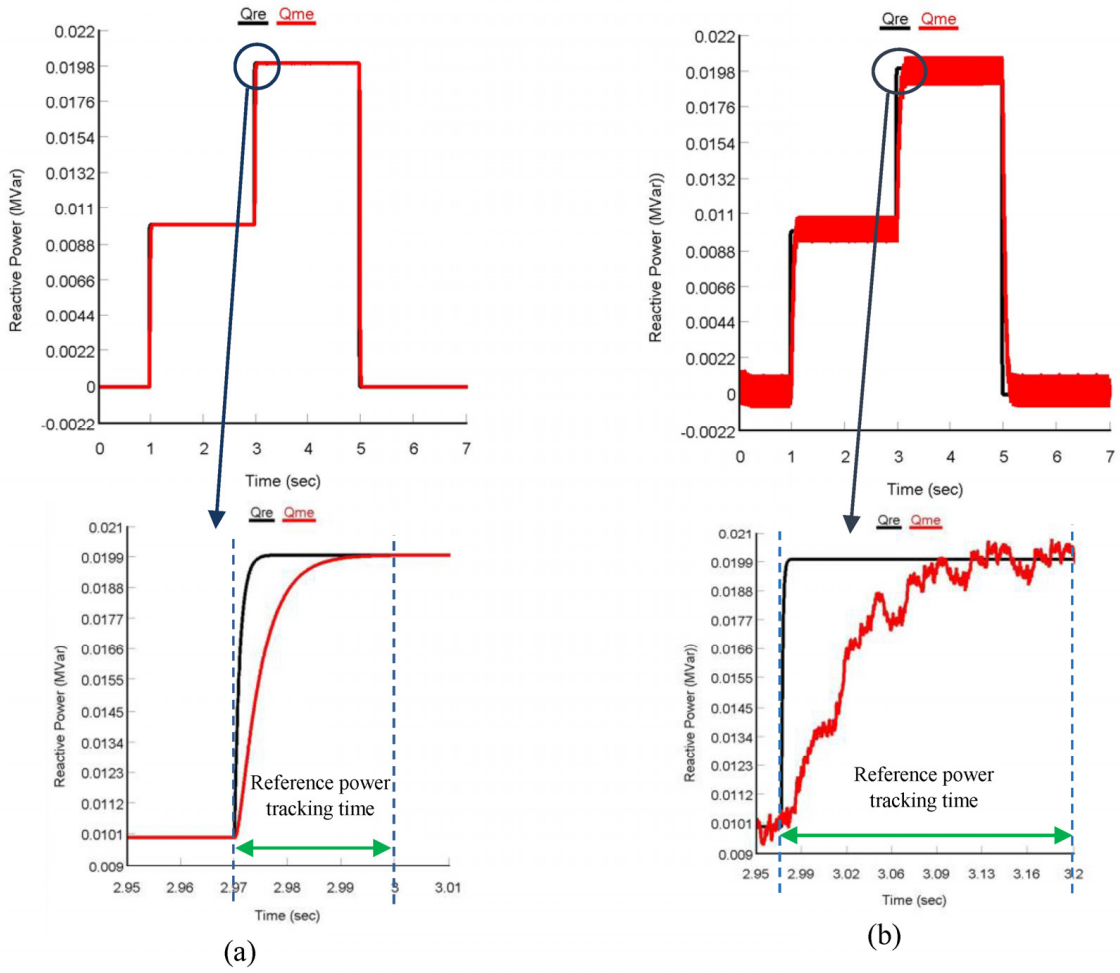

Figure 8. Reactive power tracking performance of (**a**) FLDPC method and (**b**) dq CCS based power controller with PLL.

5.1.2. Proposed Controller Steady-State Performance Analysis

In this section, the steady-state performance of the proposed PVMT-based FLDPC method is validated. From the results shown in Figures 9 and 10, it is clear that due to the use of the proposed PVMT-based FLDPC method, the ripples at VSI output power were significantly reduced. The time range considered for viewing the ripples in VSI output real and reactive power was 2.88–5 s. From Figure 9a, it can be observed that for the proposed PVMT-based FLDPC, very low ripple existed in the VSI real power output. However, a higher ripple was observed in the VSI real power output for the conventional PLL-based power controller, which ranged between 0.0984 and 0.1006 MW. Real power also did not follow the reference accurately, as seen from Figure 9b. For reactive power, it can be seen from Figure 10b that the ripple was very high for the conventional CCS-based power controller and it ranged from 0.019 to 0.0208 MVar. On the other hand, for the proposed PVMT-based FLDPC method, reactive power also had very low power ripple, as shown in Figure 10a.

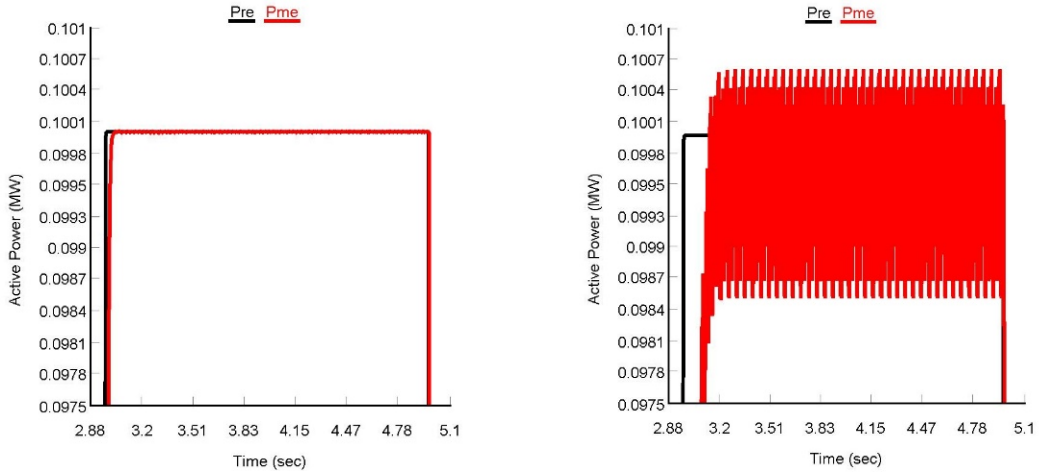

Figure 9. Real power steady-state performance of (**a**) FLDPC and (**b**) dq CCS-based power control method with PLL.

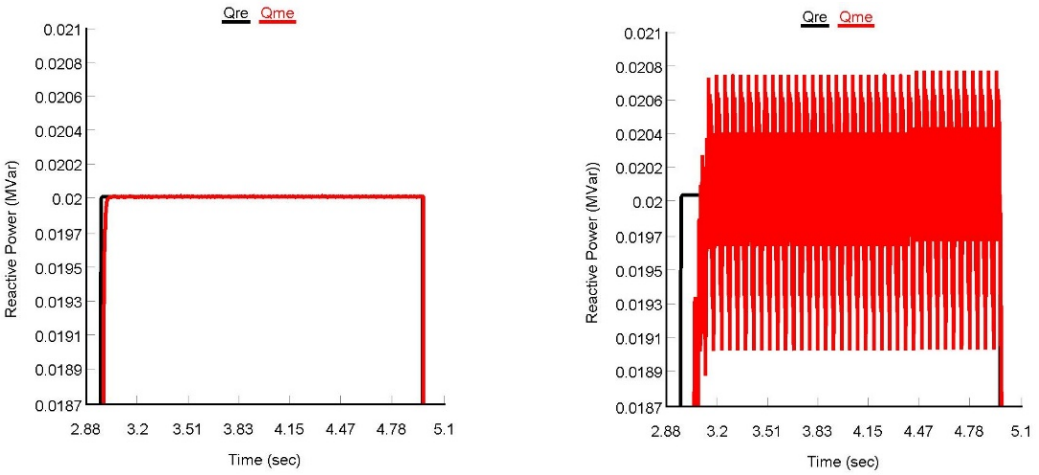

Figure 10. Reactive power steady-state performance of (**a**) FLDPC and (**b**) dq CCS-based power control method with PLL.

In Figures 11 and 12, the waveforms of the PV-VSI's output current and voltage are presented for both the controllers. From Figures 11a and 12a, it can be seen that for PLL-less PVMT-based FLDPC, the PV-VSI output voltage and current were sinusoidal in shape, and had negligible noises. In comparison, even though the PV-VSI output voltage and current for PLL-integrated CCS-based power controller were sinusoidal in shape, large distortion was observed, as shown in Figures 11b and 12b.

Further from Figure 13, it was observed that for both the controllers, the THD of the PV-VSI currents was less than 5%, which is in line with the IEC standard [44]; however, the current THD (4.967%) obtained by the PLL-CCS-based power control method was very high, compared with the PVMT-based FLDPC method's current THD (1.59%). As a result, oscillations in PV-VSI output power and current during steady-state were very low for PLL-less PVMT-based FLDPC, compared with the power control method based on PLL-integrated dq CCS.

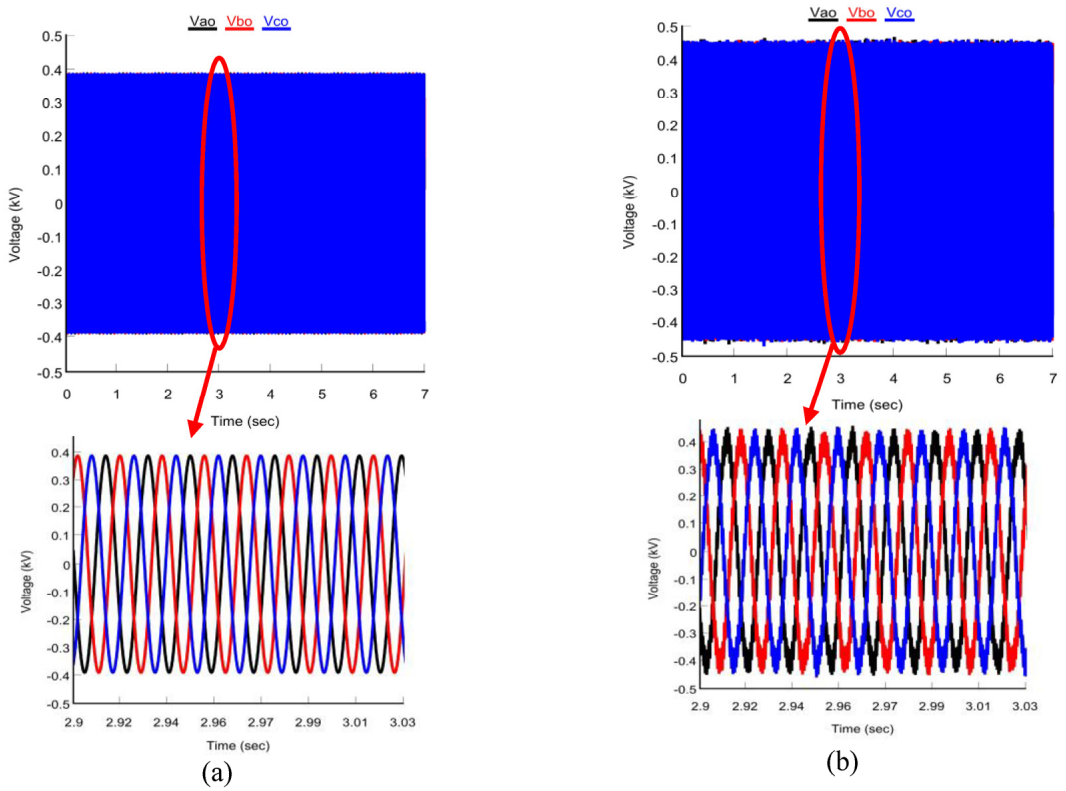

Figure 11. PV-VSI output voltage for (**a**) FLDPC method and (**b**) dq CCS-based power controller with PLL.

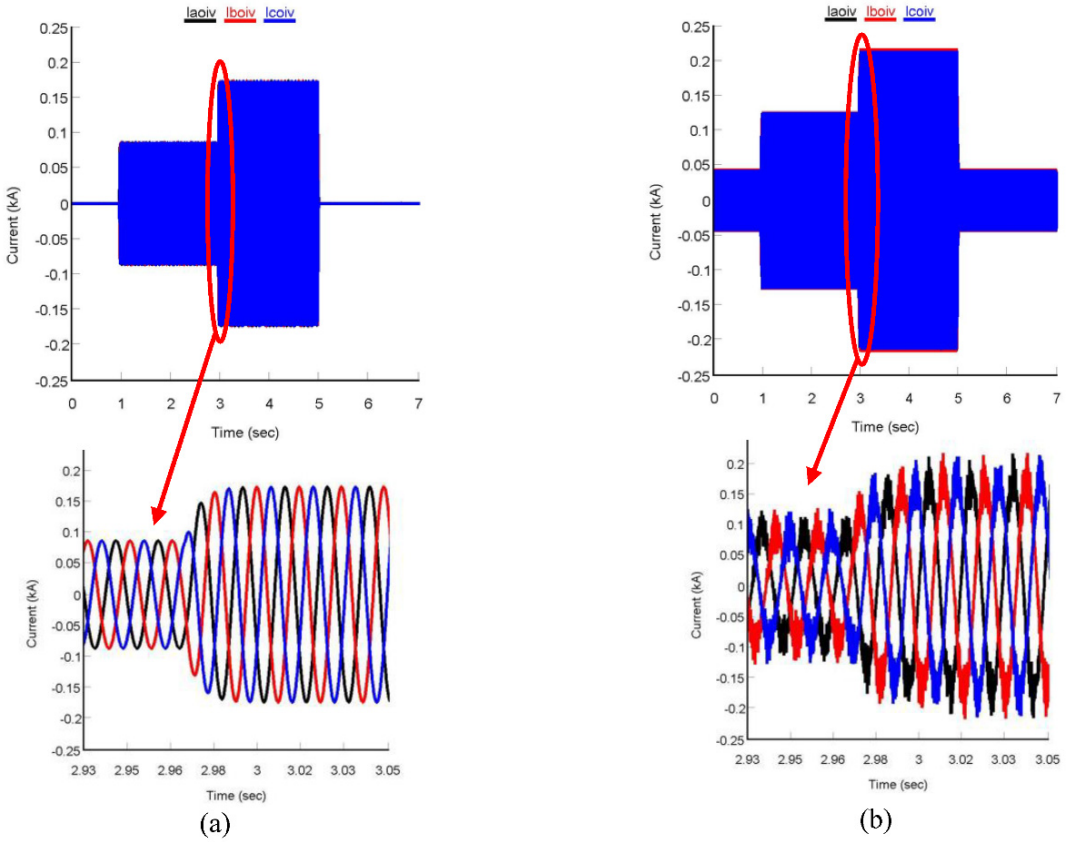

Figure 12. PV-VSI output current for (**a**) FLDPC method and (**b**) dq CCS-based power controller with PLL.

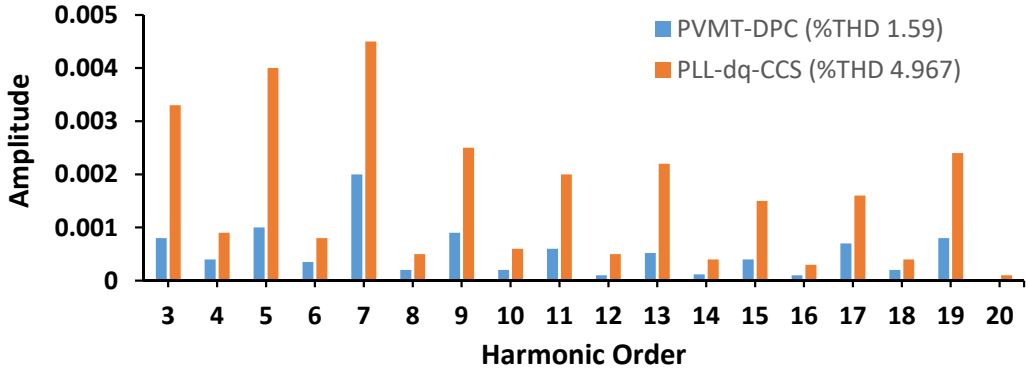

Figure 13. VSI output current THD for FLDPC and dq CCS-based power control method.

5.2. Case 2: Proposed Controllers Performance Analysis in Grid-Tied AC MG Application

It was essential to analyze the performance of the proposed PVMT-based FLDPC in grid-tied AC-MGs, to ensure that the controller was performing well in MG's different operating modes. In addition, the controller should be capable of operating in different real-world conditions such as varying load, and solar irradiation in MG. To verify these features in this section, the performance of the proposed PVMT-based FLDPC method was validated by varying both solar irradiation and load demand. Finally, a comparison is presented at the end of this section, to prove the superiority of the proposed FLDPC method over conventional MG power control methods for grid-tied VSIs. The results obtained after implementing the proposed controller for active power flow between different sources and loads are depicted in Figure 14 and Table 2. To regulate the power flow between different sources and load, a power management algorithm was adopted from [17].

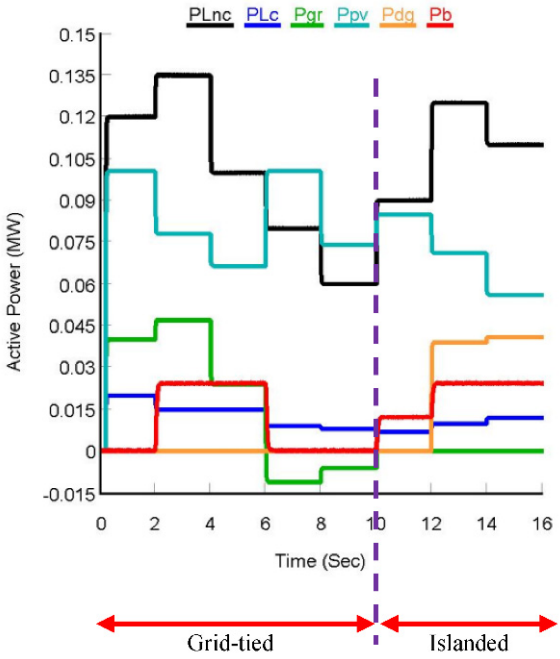

Figure 14. Active power flow from different power sources to loads.

The initial values of solar irradiation and varying load were set to 1000 W/m^2 and 0.14 MW (critical 0.02 MW + non-critical 0.12 MW, respectively). In between 0 and 2 s, PV was generating full power of 0.1 MW, which fulfilled 0.1 MW of the total load, and the remaining 0.04 MW demand was supplied by grid. At this period, the power from battery and diesel generator were nil. The solar irradiation was dropped to 850 W/m^2 between 2 and 4 s and, in contrast, load demand was increased to 0.15 MW. During this

period, PV provided a maximum of 0.078 MW power support to the load. Since PV power went down from the nominal value, the battery came into operation. In this case, the battery and grid supplied 0.025 MW and 0.047 MW power to fulfil the rest of the load demand. From 4 to 6 s, solar irradiation and load demand reduced to 700 W/m^2 and 0.115 MW, respectively. This situation compelled the grid to supply power of 0.024 MW to the load, since PV (0.066 MW) and battery (0.025 MW) together can support a maximum of 0.091 MW power. During 6–8 s, load demand decreased (0.089 MW) and solar irradiation increased (1000 W/m^2). Since the total load demand (0.089 MW) was less than the PV generation (0.1 MW), the remaining power (0.011 MW) from MG was delivered towards grid, and power from battery became zero. At 8 s, solar irradiation level reached 800 W/m^2 and the PV system generated a power of 0.074 MW. During 8–10 s, the load demand was 0.068 MW, which was supplied by the PV system fully, and remaining power (0.006 MW) of MG was supplied to the grid. For this period, power obtained from battery was nil and from 0 to 10 s, since MG was operating in grid-tied mode; therefore, the diesel generator did not provide any power support. The MG started operating in islanded mode at 10 s when the grid disconnected from the MG. During islanding, according to the power management algorithm, if PV and battery cannot fulfill the load demand, then the diesel generator will be activated. From 10 to 12 s, the generation of the PV system was 0.085 MW while the load demand was higher than the PV generation, i.e., 0.097 MW. As the battery had enough power (0.012 MW) to fulfil the remaining load demand, the diesel generator remained inactive during this duration. After 12 s, solar irradiation was reduced to 800 W/m^2 and load demand increased to 0.13 MW. During 12–14 s, the total generation (0.096 MW) from solar and battery (0.071 MW + 0.025 MW) was not sufficient to support the load demand. As a result, diesel generation turned on and supplied 0.034 MW power to fulfil the remaining load demand. Lastly, between 14 and 16 s, the PV generation further reduced to 0.056 MW. However, load demand did not reduce much (0.122 MW), which compelled the diesel generator to continue the power supply as PV, and the battery could not fulfill the total load demand.

Table 2. Summary of active power flow from different power sources to loads.

Duration (s)	Variables		Demand		Generation			
	Solar Irradiaion (W/m^2)	Total Load (MW)	Critical Load, P_{Lc} (MW)	Non-Critical Load, P_{Lnc} (MW)	Grid, P_{gr} (MW)	Solar, P_{pv} (MW)	Diesel Genrator, P_{dg} (MW)	Battery, P_b (MW)
0–2	1000	0.14	0.02	0.12	0.04	0.1	0	0
			Total = 0.14				**Total = 0.14**	
2–4	850	0.15	0.015	0.135	0.047	0.078	0	0.025
			Total = 0.15				**Total = 0.15**	
4–6	700	0.115	0.015	0.1	0.024	0.066	0	0.025
			Total = 0.115				**Total = 0.115**	
6–8	1000	0.089	0.009	0.08	−0.011	0.1	0	0
			Total = 0.089				**Total = 0.089**	
8–10	800	0.068	0.008	0.06	−0.006	0.074	0	0
			Total = 0.068				**Total = 0.068**	
10–12	900	0.097	0.007	0.09	0	0.085	0	0.012
			Total = 0.097				**Total = 0.097**	
12–14	750	0.13	0.01	0.12	0	0.071	0.034	0.025
			Total = 0.13				**Total = 0.13**	
14–16	600	0.122	0.012	0.11	0	0.056	0.041	0.025
			Total = 0.122				**Total = 0.122**	

In Figures 15 and 16, the output power, current and voltages of PV and battery VSIs are presented. Figure 15a shows that through the PV-VSI, the amount of delivered power was almost same as the power supplied by the PV with low ripple. In addition, the PV-VSI output current also had less distortion, as shown in Figure 15b, because the PVMT-based

FLDPC was implemented to control the PV-VSI. Similarly, from Figure 15c, it can be observed that the PV-VSI output voltage also had a pure sine wave shape, and negligible ripple. On the other hand, due to the use of PLL-integrated CCS-based controller battery VSI output power, current and voltage had high steady-state oscillations and distortions, which are presented in Figure 16a–c, respectively.

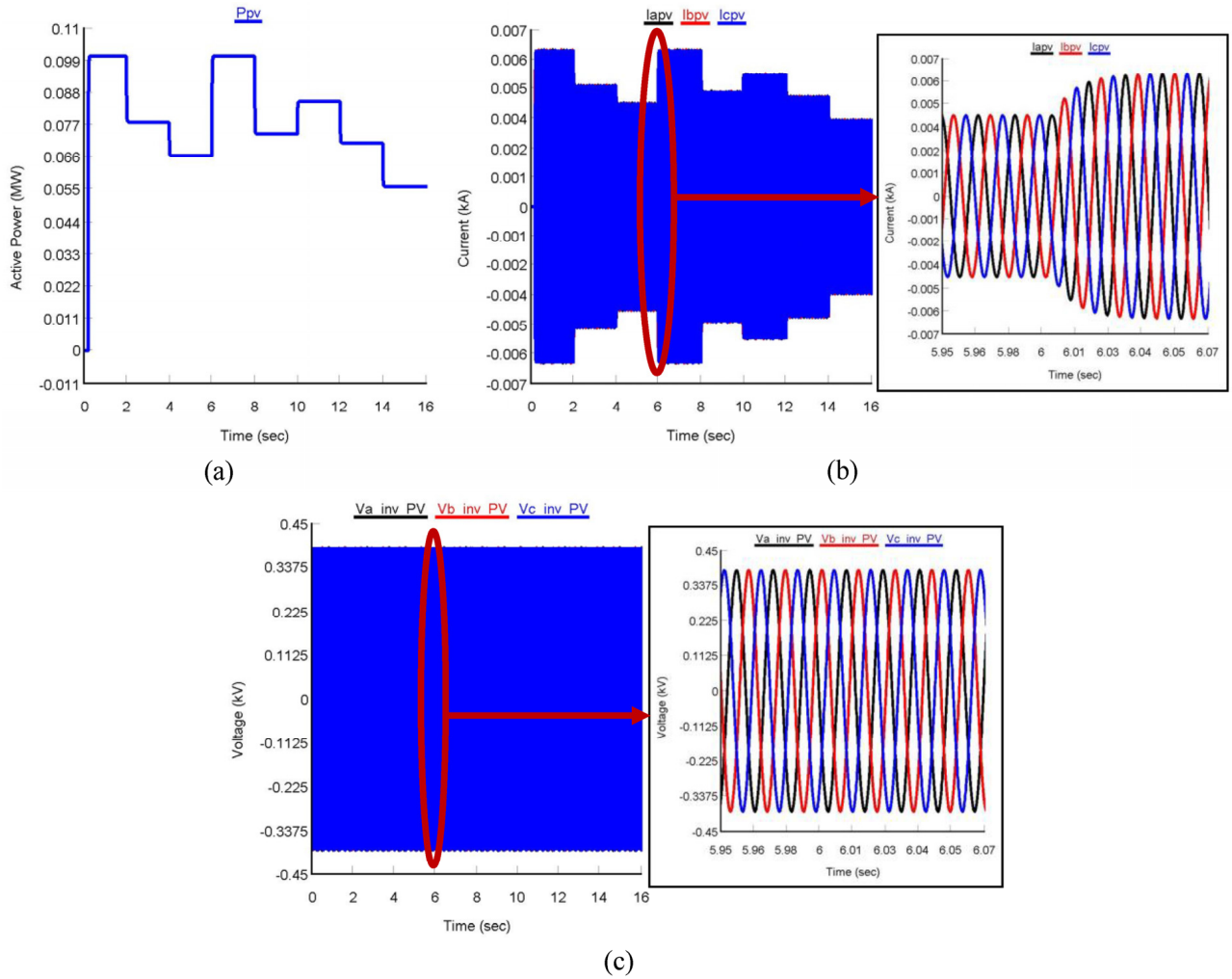

Figure 15. AC MG's PV-VSI output (**a**) power, (**b**) current and (**c**) voltage during solar irradiation and load changes.

The THD of PV and battery VSIs' output currents and voltages are depicted in Figure 17a–c, respectively. From the figures, it can be seen that the THD of PV-VSI output current was only 1.585%, whereas battery VSI output current THD was 4.718%, which was higher compared with PV-VSI current THD. In the case of voltages, battery VSI output voltage THD (2.592%) was higher than the PV-VSI output voltage THD (1.44%). The THDs were measured by considering three cycles (5.95–6 s) of current and voltage waveforms, as shown in the zoomed portion of Figure 15b,c and Figure 16b,c. Finally, in Figure 18a–c, grid power, current and voltage are presented, respectively. From the figures, it is clear that the power delivered or absorbed by the grid was according to the MG's requirement, and there were negligible ripples observed in the power. Furthermore, the shape of grid current and voltage were sinusoidal, which maintained 60 Hz frequency and had no distortions.

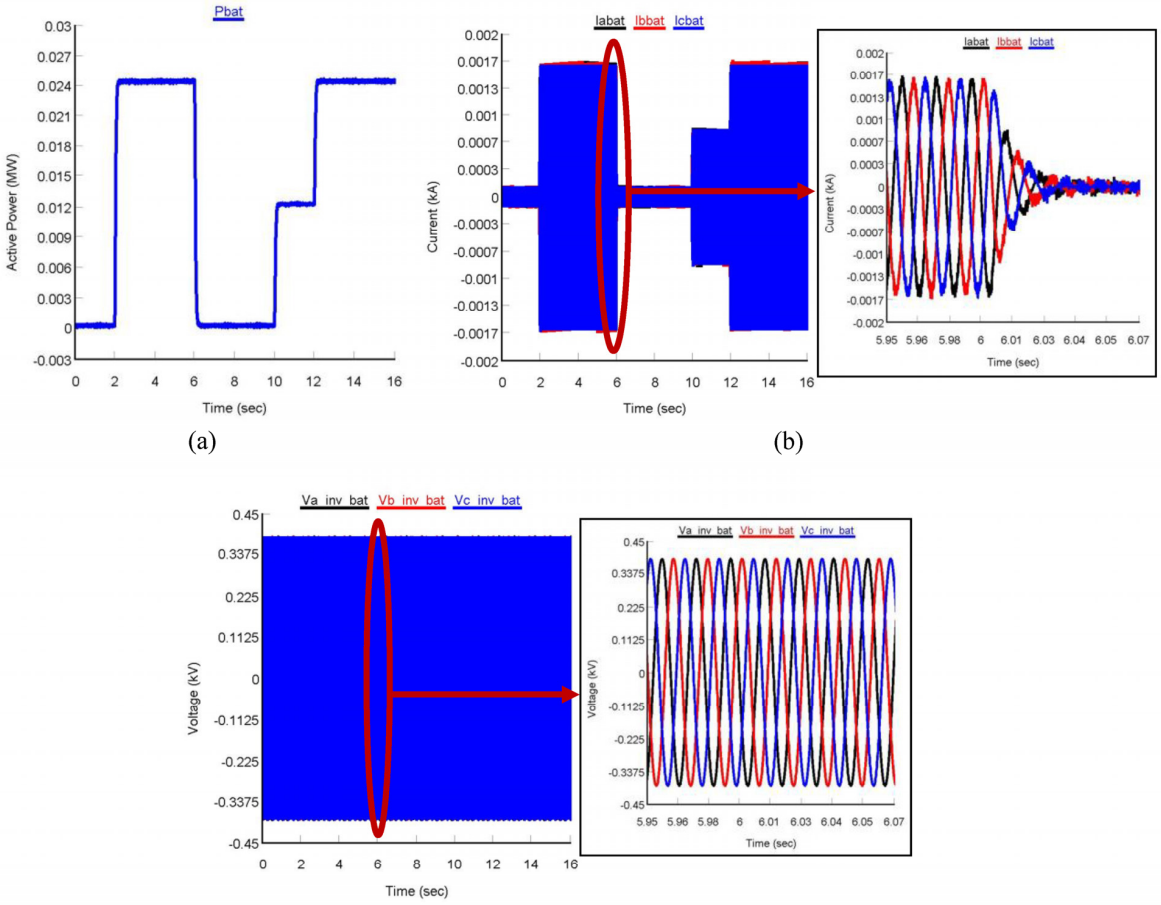

Figure 16. AC-MG's battery VSI output (**a**) power, (**b**) current and (**c**) voltage during solar irradiation and load changes.

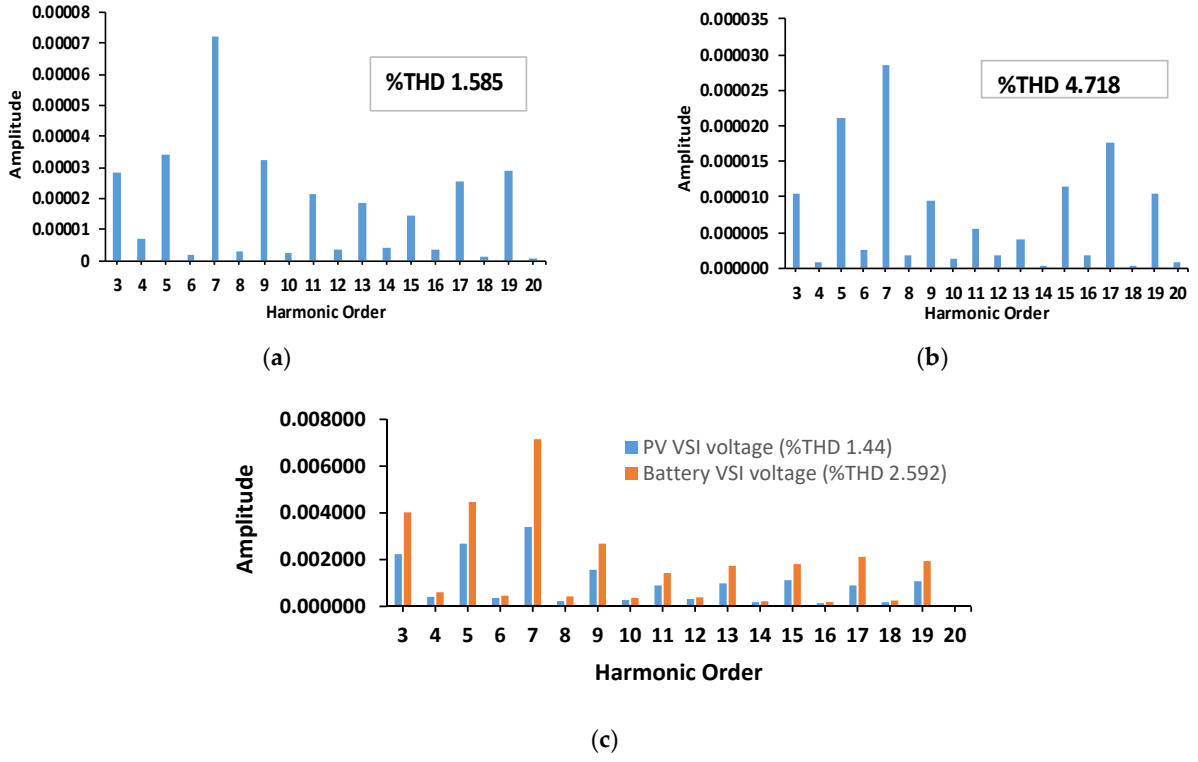

Figure 17. THD of (**a**) PV-VSI output current and (**b**) battery VSI output current and (**c**) PV and battery VSIs output voltage.

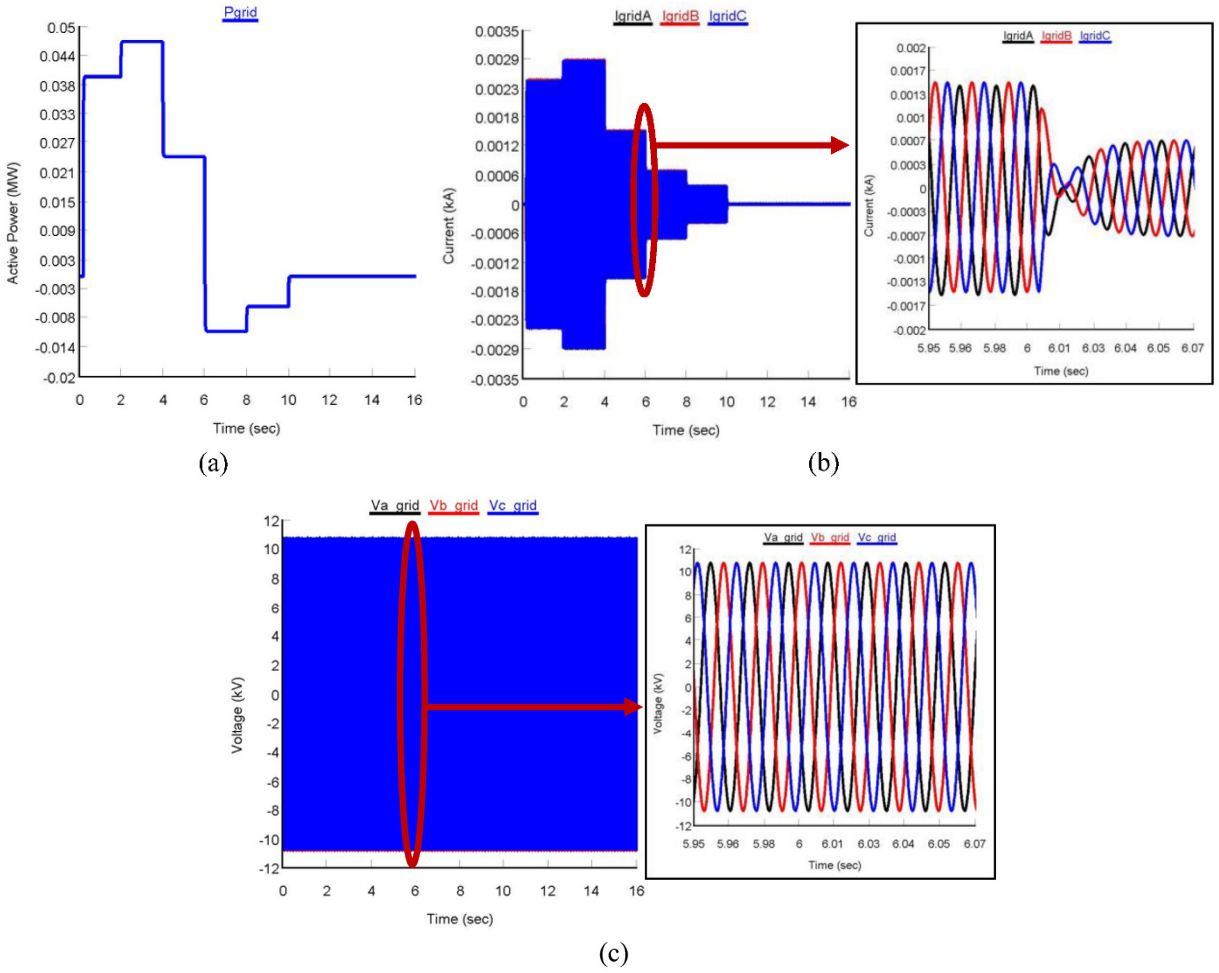

Figure 18. Grid (**a**) power, (**b**) current and (**c**) voltage during solar irradiation and load changes.

5.3. Comparison of the Proposed PVMT-Based FLDPC with Other MG Power Controllers

In this section, a comparative study is conducted between the proposed PLL-less PVMT-based FLDPC method and other grid-tied MG power control methods from [5–7,9,11]. The controllers were modelled in RSCAD, and their performances were tested by implementing them for controlling PV-VSI, as shown in Figure 1. The results were obtained by conducting real-time simulations in RTDS, and to make a fair comparison during simulations, all the parameters of MG were set similarly. The results of the comparative study are presented in Table 3 which shows that the proposed PVMT-based FLDPC method exhibited better performance than the other MG power control methods.

All the results are presented for the period of 1–2 s, when AC-MG was operating in grid-tied mode. For instance, the reference power tracking time of the proposed DPC controller was 0.20 s, 0.195 s, 0.185 s, 0.12 s, 0.14 s and 0.19 s faster than the controllers proposed in [5–7,9,11], respectively. Moreover, the PV-VSI output current THD was observed as 1.585%, approximately in the range of 2.264% to 3.289% lesser compared with the controllers in [5–7,9,11]. Furthermore, the power ripple in the output of PV-VSI controller by the proposed FLDPC was very low compared with the ripples that existed in the output power of PV-VSIs regulated by the controllers proposed in [5–7,9,11].

Table 3. Comparative analysis of the proposed PVMT-based FLDPC with other MG power controllers.

#	MG Power Controller	PLL System Presence	Active Power Ripples Range	Reference Power Tacking Time (s)	THD of VSI Output Voltage (%)	THD of VSI Output Current (%)
1	**Proposed PVMT-based FLDPC**	**No**	**Very small (0.09999–0.10 MW)**	**0.03**	**1.44**	**1.585**
2	Ref [5]	Yes	Large (0.0983–0.101 MW)	0.23	3.91	4.975
3	Ref [6]	Yes	Large (0.098–0.102 MW)	0.225	3.85	4.967
4	Ref [7]	Yes	Large (0.0985–0.1009 MW)	0.215	3.83	4.87
5	Ref [9]	Yes	Medium (0.0994–0.1003 MW)	0.15	2.59	3.95
6	Ref [11]	Yes	Large (0.0986–0.1009 MW)	0.22	3.80	4.76
7	Ref [27]	Yes	Medium (0.0993–0.1004 MW)	0.14	2.55	3.92

6. Discussion

From the real-time simulation results, it can be realized that the proposed PLL-less PVMT-based FLDPC method is capable of controlling the real and reactive power, irrespective of the load variability and solar irradiation variations. For different power references, it was observed that the PV-VSI output real power controlled by the proposed PVMT-based FLDPC was tracking the reference real and reactive powers accurately. On the other hand, though the conventional dq CCS-based power controller was also tracking the reference powers, the tracking speed of the proposed PLL-less PVMT-based FLDPC method was found to be faster than that of the conventional dq CCS-based power control method, because the proposed power control method PLL system and park transformation was omitted and the PCC voltage modulated the DPC method. Moreover, in the feedback controller, FLC was applied to minimize the errors between the reference powers and VSI output power, to ensure PV-VSI output powers were following the reference powers accurately.

Similar to the tracking performance the proposed PLL-less PVMT-based FLDPC method exhibited excellent performance during a steady-state. The proposed PVMT-based FLDPC overcame the steady-state oscillations issue, due to acquirement of an exponentially stable decoupled linear time invariant error dynamic by the proposed controller. It was observed that for the proposed PVMT-based FLDPC, there was very low ripple in the VSI real and reactive power output. However, there was higher ripple observed in the VSI power outputs for the conventional PLL-based power controller, and powers were also not following the reference accurately.

From the results presented in Table 2, it can be seen that the proposed controller also performed as outstanding while transferring power among different sources of MG, grid and load during MG's grid-tied, and islanding operating modes. From the real time simulation results, it was observed that during grid-tied mode the proposed PVMT-DPC method performed excellently by maintaining the required power flow between the MG and grid, as the PV system was capable of providing the power according to the solar irradiation changes. In addition, during the transition from grid-connected to islanded mode, the proposed PVMT-DPC method also showed a robust performance. Finally, from the comparison results presented in Table 3, it was observed that the proposed PLL-less PVMT-based FLDPC method integrated PV-VSI showed a better performance during both

the transient-state and the steady-state compared with the conventional power controller-integrated PV-VSIs connected to AC-MGs.

7. Conclusions

In this paper, a FLDPC scheme based on PVMT for a grid-tied MG's PV-VSI was introduced. The performance of the proposed power controller was validated by conducting real-time simulations using RTDS for two cases varying in both real and reactive power references, and in AC-MGs different operating modes. For case-1, the tracking and steady-state performance of the proposed FLDPC for a grid-tied PV-VSI was validated by changing real and reactive power references. On the other hand, for case-2 the performance of the proposed controller was validated for AC-MG's PV-VSI by varying the solar irradiation and load demand.

For case-1, real-time simulation results show that the proposed FLDPC method was able to track both real and reactive power to their reference powers accurately and quickly. The reference power tracking time required by the proposed FLDPC method for both real and reactive power was only 0.03 s, whereas the conventional PLL-integrated dq CCS-based power controller took 0.23 s, which was 0.20 s slower than the proposed controller. The proposed controller during steady-state also demonstrated outstanding performance as the ripples in the PV-VSI output power significantly reduced, and the THD of VSI output current achieved was 1.59%, which was well below the 5% set by the IEC standard. On the contrary, for a conventional PLL-integrated dq CCS-based power controller, the THD of VSI output current obtained was very high (4.975%) compared with the proposed FLDPC method.

Furthermore, for case-2, in MG application (grid-tied, and islanded operating modes), the proposed FLDPC method of PV-VSI showed an outstanding performance during the variation of solar irradiance and load. From the real-time simulation results, it was observed that during the grid-tied mode the proposed PVMT-based FLDPC method has performed excellently, by maintaining the required power flow between the MG and grid. Finally, a comparative study was conducted to prove the superiority of the proposed FLDPC method, with respect to other grid-tied MG power control methods. It was observed that the proposed FLDPC method outperformed all the other controllers, having a PI-based feedback controller and PLL-based synchronization methods, along with two control loops for parameters such as power ripples, THD and reference power tracking time.

In this work, the performance of the proposed FLDPC method was validated on AC-MG, which was connected to a healthy utility grid. In future, the performance of the FLDPC will also be validated for distorted grid conditions. Furthermore, for the grid re-synchronization process, the performance of the proposed FLDPC method was not validated. This will be conducted in the future.

Author Contributions: Conceptualization and methodology, S.A. (Shameem Ahmad) and M.K.; simulation and validation, S.A. (Shameem Ahmad), U.K.J., S.A. (Suhail Afzal) and A.P.; manuscript writing and editing, S.A. (Shameem Ahmad), S.M., H.M., M.K., S.A. (Suhail Afzal) and T.A.; supervision, S.M. and H.M. All authors have read and agreed to the published version of the manuscript.

Funding: This work was financially supported by the Academy of Finland under the project number Profi4/WP2. Some parts of this work were done in the SolarX research project with the financial support provided by the Business Finland with Grant No. 6844/31/2018. The financial support provided through these research projects is highly acknowledged.

Data Availability Statement: The data used in this research is enclosed within the manuscript. No external data sources are used in this research.

Conflicts of Interest: The authors declare no conflict of interest.

Nomenclature

VSI	Voltage source inverter
MG	Microgrid
PLL	Phase locked loop
DPC	Direct power control
FLC	Fuzzy logic controller
RTDS	Real time digital simulator
CCS	Current control scheme
PI	Proportional Integral
SOC	State of Charge
PVM	PCC voltage modulation
FLDPC	Fuzzy logic direct power control
PV	Photovoltaic
MPPT	Maximum power point tracker
BSS	Battery storage system
THD	Total harmonic distortion
SPWM	Sinusoidal pulse width modulation
MI	Modulation index
PCC	Point of common coupling
PVMT	PCC voltage modulation theory
ANN	Artificial neural network

Appendix A

Table A1. Parameters of AC MG components [38].

Parameters	Value
PV System (0.1 MW)	
PV modules connected in series	28
PV modules connected in parallel	68
Solar irradiation reference value	1000 W/m^2
Voltage at maximum power	17.3 V
Voltage at open circuit	21.5 V
Current at maximum power	3.05 A
PV module Temperature	25 °C
Current during short circuit (I_{sc})	3.33 A
Battery Storage (25 kWh)	
Nominal voltage per cell	3.6 V
Initial SOC of each cell	90%
Capacity of each cell	0.85 AH
State of charge (SOC) of battery	Greater than 60%
Cells connected in parallel	290
Cells connected in series	135
Diesel Generator (0.15 MVA)	
Machine power rating	0.15 MVA
Line to line voltage	0.48 kV

Table A1. *Cont.*

Parameters	Value
Grid	
Transformer primary/secondary voltage	0.48 kV/13.2 kV
Grid Voltage	13.2 kV
Frequency	60 Hz
Load	
Non-critical load	0.05–0.14 MW
Critical Load	0.005–0.015 MW
PV-VSI	
Voltage at DC link	975 V
PV-VSI switching frequency	2 kHz
DC-link capacitor	500 µF
$R_{a,b,c}$	0.1 Ω
$L_{a,b,c}$	5 mH
Battery VSI	
Voltage at DC link	975 V
PV-VSI switching frequency	2 kHz
DC-link capacitor	450 µF
$R_{a,b,c}$	0.01 Ω
$L_{a,b,c}$	5.5 mH
DC-DC Buck-Boost Converter (Battery Storage)	
Switching frequency	20 kHz
Capacitance	74 µF
Inductance	6 mH
DC-DC Boost Converter (PV System)	
Switching frequency	20 kHz
Capacitance	85 µF
Inductance	8 mH

Table A2. Values of PI controller coefficients for DC-link control.

Coefficients	Value
$K_{i,dc}$	0.015
$K_{p,dc}$	10

References

1. Bullich-Massagué, E.; Aragüés-Peñalba, M.; Prieto-Araujo, E.; Sumper, A.; Caire, R. Optimal feeder flow control for grid connected microgrids. *Int. J. Electr. Power Energy Syst.* **2019**, *112*, 144–155. [CrossRef]
2. Borhanazad, H.; Mekhilef, S.; Ganapathy, V.G.; Modiri-Delshad, M.; Mirtaheri, A. Optimization of micro-grid system using MOPSO. *Renew. Energy* **2014**, *71*, 295–306. [CrossRef]
3. Worku, M.Y.; Hassan, M.A.; Abido, M.A. Real time-based under frequency control and energy management of microgrids. *Electronics* **2020**, *9*, 1487. [CrossRef]
4. Hossain, M.A.; Pota, H.R.; Hossain, M.J.; Blaabjerg, F. Evolution of microgrids with converter-interfaced generations: Challenges and opportunities. *Int. J. Electr. Power Energy Syst.* **2019**, *109*, 160–186. [CrossRef]

5. Worku, M.Y.; Hassan, M.A.; Abido, M.A. Real time energy management and control of renewable energy based microgrid in grid connected and island modes. *Energies* **2019**, *12*, 276. [CrossRef]
6. Safa, A.; Berkouk, E.M.; Messlem, Y.; Gouichiche, A. A robust control algorithm for a multifunctional grid tied inverter to enhance the power quality of a microgrid under unbalanced conditions. *Int. J. Electr. Power Energy Syst.* **2018**, *100*, 253–264. [CrossRef]
7. Kaushal, J.; Basak, P. Power quality control based on voltage sag/swell, unbalancing, frequency, THD and power factor using artificial neural network in PV integrated AC microgrid. *Sustain. Energy Grids Netw.* **2020**, *23*, 100365. [CrossRef]
8. Smadi, I.A.; Albatran, S.; Alsyouf, M.A. Optimal control of a compact converter in an AC microgrid. *Electronics* **2018**, *7*, 102. [CrossRef]
9. Lou, G.; Gu, W.; Zhu, J.; Li, P.; Zhang, X. A novel control strategy for the seamless transfer of microgrids based on disturbance observer. *Int. J. Electr. Power Energy Syst.* **2020**, *118*, 105804. [CrossRef]
10. Abadlia, I.; Adjabi, M.; Bouzeria, H. Sliding mode based power control of grid-connected photovoltaic-hydrogen hybrid system. *Int. J. Hydrogen Energy* **2017**, *42*, 28171–28182. [CrossRef]
11. Feng, W.; Sun, K.; Guan, Y.; Guerrero, J.M.; Xiao, X. Active power quality improvement strategy for grid-connected microgrid based on hierarchical control. *IEEE Trans. Smart Grid* **2016**, *9*, 3486–3495. [CrossRef]
12. Adhikari, S.; Li, F. Coordinated Vf and PQ control of solar photovoltaic generators with MPPT and battery storage in microgrids. *IEEE Trans. Smart Grid* **2014**, *5*, 1270–1281. [CrossRef]
13. Mousavi, S.Y.M.; Jalilian, A.; Savaghebi, M.; Guerrero, J.M. Coordinated control of multifunctional inverters for voltage support and harmonic compensation in a grid-connected microgrid. *Electr. Power Syst. Res.* **2018**, *155*, 254–264. [CrossRef]
14. Go, S.-I.; Choi, J.-H. Design and dynamic modelling of pv-battery hybrid systems for custom electromagnetic transient simulation. *Electronics* **2020**, *9*, 1651. [CrossRef]
15. Sedaghati, R.; Shakarami, M.R. A novel control strategy and power management of hybrid PV/FC/SC/battery renewable power system-based grid-connected microgrid. *Sustain. Cities Soc.* **2019**, *44*, 830–843. [CrossRef]
16. Tang, X.; Zhang, D.; Xiao, D.; Li, M. Modeling and Stability Analysis of a Novel Voltage-Oriented Power Coordination Controlled Constant-Frequency AC Microgrid System. *Electronics* **2021**, *10*, 1935. [CrossRef]
17. Ahmad, S.; Mekhilef, S.; Mokhlis, H. DQ-axis Synchronous Reference Frame based PQ Control of Grid Connected AC Microgrid. In Proceedings of the 2020 IEEE International Conference on Computing, Power and Communication Technologies (GUCON), Greater Noida, India, 2–4 October 2020; pp. 842–847.
18. Lee, L.A.; Liu, C.C.; Xu, Y.; Schneider, K.P.; Tuffner, F.K.; Mo, K.; Ton, D.T. Dynamics and control of microgrids as a resiliency source. *Int. Trans. Electr. Energy Syst.* **2020**, *30*, e12610. [CrossRef]
19. Ali, Z.; Christofides, N.; Hadjidemetriou, L.; Kyriakides, E.; Yang, Y.; Blaabjerg, F. Three-phase phase-locked loop synchronization algorithms for grid-connected renewable energy systems: A review. *Renew. Sustain. Energy Rev.* **2018**, *90*, 434–452. [CrossRef]
20. Wang, X.; Harnefors, L.; Blaabjerg, F. Unified impedance model of grid-connected voltage-source converters. *IEEE Trans. Power Electron.* **2017**, *33*, 1775–1787. [CrossRef]
21. Wang, X.; Blaabjerg, F. Harmonic stability in power electronic-based power systems: Concept, modeling, and analysis. *IEEE Trans. Smart Grid* **2018**, *10*, 2858–2870. [CrossRef]
22. Harnefors, L.; Wang, X.; Yepes, A.G.; Blaabjerg, F. Passivity-based stability assessment of grid-connected VSCs—An overview. *IEEE J. Emerg. Sel. Top. Power Electron.* **2015**, *4*, 116–125. [CrossRef]
23. Gui, Y.; Kim, C.; Chung, C.C. Grid voltage modulated direct power control for grid connected voltage source inverters. In Proceedings of the 2017 American Control Conference (ACC), Seattle, WA, USA, 24–26 May 2017; pp. 2078–2084.
24. Hasanien, H.M.; Matar, M. A fuzzy logic controller for autonomous operation of a voltage source converter-based distributed generation system. *IEEE Trans. Smart Grid* **2014**, *6*, 158–165. [CrossRef]
25. Heydari, R.; Gheisarnejad, M.; Khooban, M.H.; Dragicevic, T.; Blaabjerg, F. Robust and fast voltage-source-converter (VSC) control for naval shipboard microgrids. *IEEE Trans. Power Electron.* **2019**, *34*, 8299–8303. [CrossRef]
26. Thao, N.G.M.; Uchida, K. Control the active and reactive powers of three-phase grid-connected photovoltaic inverters using feedback linearization and fuzzy logic. In Proceedings of the 2013 Australian Control Conference, Perth, Australia, 4–5 November 2013; pp. 133–140.
27. Omar, M.; El-Deib, A.; El Shafei, A.; Abdallah, M. Comparative study between PI and fuzzy-logic controllers for three-phase grid-connected photovoltaic systems. In Proceedings of the 2016 Eighteenth International Middle East Power Systems Conference (MEPCON), Cairo, Egypt, 27–29 December 2016; pp. 380–386.
28. Jamma, M.; Bennassar, A.; Barara, M.; Akherraz, M. Advanced direct power control for grid-connected distribution generation system based on fuzzy logic and artificial neural networks techniques. *Int. J. Power Electron. Drive Syst.* **2017**, *8*, 979. [CrossRef]
29. Islam, S.U.; Zeb, K.; Din, W.U.; Khan, I.; Ishfaq, M.; Hussain, A.; Busarello, T.D.C.; Kim, H.J. Design of robust fuzzy logic controller based on the levenberg marquardt algorithm and fault ride trough strategies for a grid-connected PV system. *Electronics* **2019**, *8*, 429. [CrossRef]
30. Shadoul, M.; Yousef, H.; Abri, R.A.; Al-Hinai, A. Adaptive Fuzzy Approximation Control of PV Grid-Connected Inverters. *Energies* **2021**, *14*, 942. [CrossRef]
31. Tahri, G.; Foitih, Z.A.; Tahri, A. Fuzzy logic control of active and reactive power for a grid-connected photovoltaic system using a three-level neutral-point-clamped inverter. *Int. J. Power Electron. Drive Syst.* **2021**, *12*, 453–462. [CrossRef]

32. Teekaraman, Y.; Kuppusamy, R.; Baghaee, H.R.; Vukobratović, M.; Balkić, Z.; Nikolovski, S. Current Compensation in Grid-Connected VSCs using Advanced Fuzzy Logic-based Fluffy-Built SVPWM Switching. *Energies* **2020**, *13*, 1259. [CrossRef]
33. Gui, Y.; Wang, X.; Blaabjerg, F. Vector current control derived from direct power control for grid-connected inverters. *IEEE Trans. Power Electron.* **2018**, *34*, 9224–9235. [CrossRef]
34. Gui, Y.; Kim, C.; Chung, C.C.; Guerrero, J.M.; Guan, Y.; Vasquez, J.C. Improved direct power control for grid-connected voltage source converters. *IEEE Trans. Ind. Electron.* **2018**, *65*, 8041–8051. [CrossRef]
35. Gui, Y.; Lee, G.H.; Kim, C.; Chung, C.C. Direct power control of grid connected voltage source inverters using port-controlled Hamiltonian system. *Int. J. Control Autom. Syst.* **2017**, *15*, 2053–2062. [CrossRef]
36. Choi, D.-K.; Lee, K.-B. Dynamic performance improvement of AC/DC converter using model predictive direct power control with finite control set. *IEEE Trans. Ind. Electron.* **2014**, *62*, 757–767. [CrossRef]
37. Gao, Y.; Ai, Q. Distributed cooperative optimal control architecture for AC microgrid with renewable generation and storage. *Int. J. Electr. Power Energy Syst.* **2018**, *96*, 324–334. [CrossRef]
38. Ahmad, S.; Mekhilef, S.; Mokhlis, H. An improved power control strategy for grid-connected hybrid microgrid without park transformation and phase-locked loop system. *Int. Trans. Electr. Energy Syst.* **2021**, *31*, e12922. [CrossRef]
39. Ahmad, S.; Rashid, M.T.; Ferdowsy, C.S.; Islam, S.; Mahmood, A.H. A technical comparison among different PV-MPPT algorithms to observe the effect of fast changing solar irradiation. In Proceedings of the 2015 IEEE International WIE Conference on Electrical and Computer Engineering (WIECON-ECE), Dhaka, Bangladesh, 19–20 December 2015; pp. 155–158.
40. Akram, U.; Khalid, M.; Shafiq, S. Optimal sizing of a wind/solar/battery hybrid grid-connected microgrid system. *IET Renew. Power Gener.* **2017**, *12*, 72–80. [CrossRef]
41. Sen, S.; Kumar, V. Microgrid modelling: A comprehensive survey. *Annu. Rev. Control* **2018**, *46*, 216–250. [CrossRef]
42. Filizadeh, S.; Gole, A.M.; Woodford, D.A.; Irwin, G.D. An optimization-enabled electromagnetic transient simulation-based methodology for HVDC controller design. *IEEE Trans. Power Deliv.* **2007**, *22*, 2559–2566. [CrossRef]
43. Ahmad, S.; Albatsh, F.M.; Mekhilef, S.; Mokhlis, H. Fuzzy based controller for dynamic Unified Power Flow Controller to enhance power transfer capability. *Energy Convers. Manag.* **2014**, *79*, 652–665. [CrossRef]
44. Photovoltaic, I. Systems. Characteristics of the Utility Interface. *IEC Std.* **2004**, *61*, 727.